

Physics-Grounded Shadow Generation from Monocular 3D Geometry Priors and Approximate Light Direction

Shilin Hu¹, Jingyi Xu¹, Akshat Dave¹, Dimitris Samaras^{1,†}, Hieu Le^{2,‡}

¹Stony Brook University ²UNC Charlotte [†]Equal Advising

{shilhu, jingyixu, dave, samaras}@cs.stonybrook.edu hle40@charlotte.edu

Abstract

Shadow generation aims to produce photorealistic shadows that are visually consistent with object geometry and scene illumination. In the physics of shadow formation, the occluder blocks some light rays casting from the light source that would otherwise arrive at the surface, creating a shadow that follows the silhouette of the occluder. However, such explicit physical modeling has rarely been used in deep-learning-based shadow generation. In this paper, we propose a novel framework that embeds explicit physical modeling—geometry and illumination—into deep-learning-based shadow generation. First, given a monocular RGB image, we obtain approximate 3D geometry in the form of dense point maps and predict a single dominant light direction. These signals allow us to recover fairly accurate shadow location and shape based on the physics of shadow formation. We then integrate this physics-based initial estimate into a diffusion framework that refines the shadow into a realistic, high-fidelity appearance while ensuring consistency with scene geometry and illumination. Trained on DESOBV2, our model produces shadows that are both visually realistic and physically coherent, outperforming existing approaches, especially in scenes with complex geometry or ambiguous lighting.

1. Introduction

Shadows are among the most visually powerful cues linking an object’s shape to its surrounding scene. Shadow generation aims to produce photorealistic shadows that are consistent with object geometry and scene illumination, benefiting various downstream tasks such as photo editing [35, 46], AR/VR applications [21, 38], and digital art [50]. Shadow generation, especially from a single image, is challenging because the 2D shape and orientation of the shadow are jointly determined by the 3D geometry of the occluding object and the cast surface, along with the 3D direction of the incident lighting. Large physical inconsistencies with

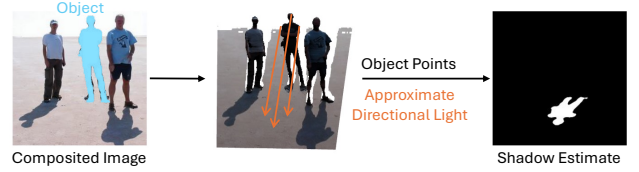


Figure 1. **Shadows estimates from approximate geometry and light direction.** Given a monocular RGB image and foreground mask, we recover approximate 3D point map and a single dominant light direction to infer a shadow estimate using object points.

the scene geometry or illumination can make the generated shadows appear unrealistic [37].

Modern deep learning methods [12, 23, 49, 51] approach the task of shadow generation purely in the 2D pixel space – where this physical relation between the shadows, geometry, and illumination is expected to *implicitly* emerge from data. This often yields inconsistencies, such as misaligned extents or incorrect orientation of the generated shadows, especially under complex geometry or ambiguous lighting. In this work, we augment learning-based generation with an *explicit* physics-based modeling of shadow formation, substantially reducing such failures.

Our physics-grounded generation has three key steps: 1) *estimating* the 3D scene geometry and 3D light direction from the composite image; 2) *rendering* an initial shadow from these estimates (Fig. 1); and 3) *conditioning* a diffusion-based generator on the initial shadow.

More specifically, our pipeline is as follows: we first compute the initial shadow estimate using the point map, the estimated light direction, and the object mask. Candidate occlusions and contacts are identified via a simple angular alignment check, retaining object–receiver pairs whose connecting ray closely aligns with the estimated light direction. These candidates provide a coarse shadow location and shape estimate. The estimate is then stacked with the denoising U-Net decoder features and passed through a coarse-to-fine mask predictor to produce a high-resolution shadow mask. During denoising, the refined shadow mask gates latent noise using scale and bias from a frozen in-



Figure 2. **Comparison with state-of-the-art shadow generation methods.** Our physics-grounded approach produces shadows that more faithfully align with the occluder geometry and scene lighting than state-of-the-art methods, SGDiffusion [23] and GPSD [51]. We evaluate both on scenes with reference object-shadow pairs in the background (BOS) and BOS-free scenes.

tensity encoder, enforcing a consistent location and shape while diffusion refines the final appearance. This design makes physical reasoning operational within a generative model, allowing geometry, illumination, and appearance to cooperate seamlessly.

We evaluate our method on DESOBAV2 [23], which contains 27,823 training and 750 testing tuples of composite images, foreground/background shadow masks, and foreground/background object masks. We obtain point maps using an off-the-shelf monocular geometry estimator [41]. Experimental results show that our method outperforms state-of-the-art approaches in generated image quality and shadow mask accuracy, producing more realistic, physically consistent shadows. As shown in Fig. 2, our method produces shadows that align faithfully with the occluder even in ambiguously lit scenes without background reference object-shadow pairs (*top*), and better preserves shadow shape and appearance under complex object geometry (*bottom*).

To summarize, our contributions are as follows:

- We propose a diffusion-based framework that integrates explicit physical modeling into shadow generation.
- We demonstrate that an initial physics-grounded estimate from monocular geometry and light estimation provides coherent shadow support for subsequent synthesis.
- Experiments show SOTA performance, with superior image quality and shadow accuracy where the shadow aligns faithfully with the occluder and light direction.

2. Related Works

Shadows have long been a fundamental focus in scene understanding [19, 20]. While shadow detection [3, 11, 13, 18, 40, 42, 52, 53] and shadow removal [4, 6, 7, 10, 12, 15–17, 17, 25, 29] primarily operate on observed image content by identifying or correcting differences between shadow and non-shadow regions, shadow generation poses a more challenging task. It requires not only synthesizing realistic shadow appearance, but also reasoning about spatial relationships to ensure consistency with scene geometry, lighting conditions, and the shape of newly inserted objects in

complex environments.

Shadow generation methods can be broadly categorized into 3D-based rendering approaches and 2D-based generative models. 3D-based methods rely on explicit scene representations—such as object geometry, lighting direction, and camera parameters—to simulate shadows via physically based rendering. Early techniques [2, 31] used depth maps and known light sources to produce soft shadow effects in screen space. More recently, Sheng *et al.* [32] replaced full 3D geometry with a manually provided pixel height map and user-specified lighting to generate controllable shadows. While accurate and physically grounded, these methods require either detailed 3D models or manual input, limiting their applicability in general image composition tasks. In contrast, 2D-based generative approaches bypass the need for explicit 3D modeling by learning to synthesize shadows directly in image space, typically conditioned on object masks or compositional cues. Liu *et al.* [22] proposed a GAN-based framework that learns a mapping from object masks to shadows, conditioned on the background appearance. Hong *et al.* [9] introduced a two-stage model that first predicts a shadow mask and then refines the shadow appearance, using an image-formation function. Most recently, [23] proposed a diffusion-based framework built on ControlNet [48] to guide shadow generation using the composite image and object mask as control signals. However, these methods overlook the physical constraints governing shadow formation, relying purely on learned image features. As a result, they often hallucinate unrealistic or inconsistent shadows.

Recent progress in depth and lighting estimation makes it feasible to recover reliable geometry and illumination from a single image. Monocular depth models perform well on diverse scenes, with [43, 44] providing strong relative depth, and [28, 45] demonstrating accurate metric depth. Illumination is commonly represented as environment maps [33, 39], light probes [1, 27], or parameterized lighting directions [5, 47]. In this work, we use the off-the-shelf MoGe-2 [41] to recover metric point maps from single images and to estimate parameterized lighting direc-

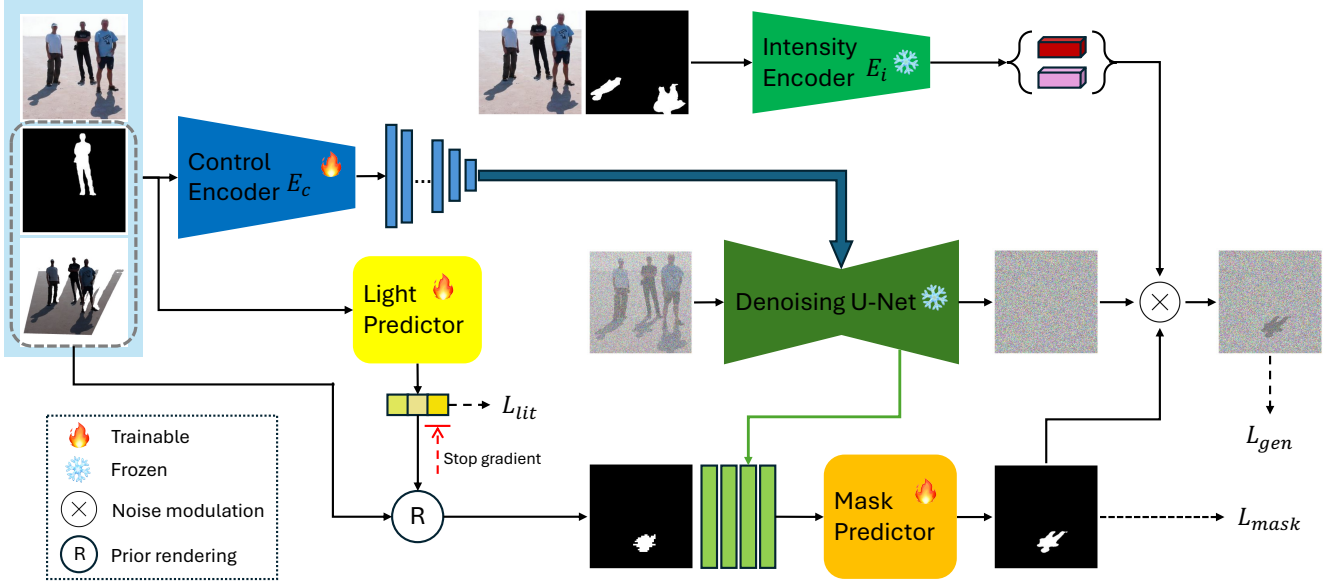


Figure 3. **Framework overview.** We inject monocular geometry by stacking the shadow-free image, foreground object mask, and dense point map as a control signal. This feeds a control encoder and a light predictor; the predictor outputs a 3D light vector to render a shadow estimate. A mask predictor fuses the shadow estimate with diffusion features to predict the shadow mask in a coarse-to-fine scheme. The denoising U-Net and the intensity encoder are frozen during training.

tions, which we then use as guidance.

Our method addresses the limitations of prior 2D-based shadow generation approaches by explicitly incorporating geometry and illumination guidance into the generation process. By adhering to the physics of shadow formation and explicitly linking occluder shape and light direction to a geometry-consistent shadow estimate, our approach yields shadows with improved shape and placement consistency relative to their occluders and scene illumination.

3. Method

Our task is to generate a physically faithful foreground shadow mask M_{fs} and the corresponding shadow image given a composite image I_c and its foreground object mask M_{fo} . Inspired by the baseline [23], our framework consists of five modules: (1) a frozen Stable Diffusion U-Net [30] for shadow image synthesis, (2) a frozen intensity encoder that predicts affine parameters for the shadow region, (3) a control encoder enriched with geometric cues, (4) a light predictor that regresses a three-dimensional light vector from the control signals, and (5) a mask predictor that estimates the foreground shadow mask. Fig. 3 shows the overall architecture. As in the baseline, we use an empty text prompt for the diffusion model by default.

3.1. Control Encoder

As shown in Fig. 3, the control encoder receives a shadow-free RGB image, a foreground object mask, and a per-pixel point map as control signals. We concatenate them to form a 7-channel input. The shadow-free image and object

mask convey scene appearance and object locality, while the dense point map augments the control with explicit geometry—encoding object-background relationships and surface layout. Together, these cues improve spatial interpretability and provide stronger guidance to the downstream modules.

3.2. Light Predictor

We estimate a scene-wide 3D light direction for the composite I_c using a lightweight ConvNeXt-Small[24] head over the control stack. The backbone processes the stack; this is followed by a global average pooling and a 2-layer MLP to regress a 3D light vector $\mathbf{l} \in \mathbb{R}^3$, and finally normalize it to a unit vector $\hat{\mathbf{l}} = \mathbf{l} / \|\mathbf{l}\|_2$. Note that our light direction is defined to point toward the source. This design yields a stable scene-level estimate while keeping computation minimal. We supervise the predicted direction with a cosine-similarity loss as follows:

$$\mathcal{L}_{lit} = 1 - \hat{\mathbf{l}} \cdot \hat{\mathbf{l}}_{gt}, \quad (1)$$

where $\hat{\mathbf{l}}_{gt}$ is the approximate ground-truth light direction obtained as described in Sec. 3.5. Because the light predictor is trained separately from the denoising path, we detach its output before feeding it to the mask predictor. Thus, denoising losses do not back-propagate into the light head, and light-loss gradients remain confined to the light head. This prevents gradient leakage between branches and ensures supervision targets the intended components.

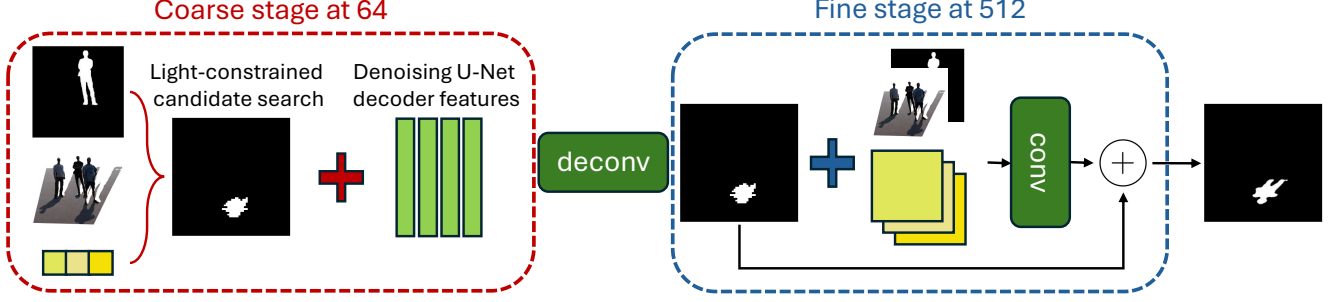


Figure 4. **Mask Predictor.** From the foreground mask M_{fo} , point map \mathbf{P} , and predicted light $\hat{\mathbf{l}}$, we form an illumination-consistent shadow estimate at 64×64 . The coarse stage stacks this estimate with denoising U-Net decoder features, upsamples to 512×512 , and the fine stage concatenates the coarse map with M_{fo} , \mathbf{P} , and a broadcast light map, then applies a residual refinement for the final mask.

3.3. Mask Predictor

Using the foreground object mask M_{fo} , the point map \mathbf{P} and the estimated light direction $\hat{\mathbf{l}}$, we follow the shadow-formation principle to derive an illumination-consistent shadow estimate. Let $\mathbf{P}(x, y) \in \mathbb{R}^3$ be the 3D point for pixel (x, y) , and let \mathcal{O} and \mathcal{R} denote the sets of object and receiver pixels, respectively. We define the flow direction as $\mathbf{D} = -\hat{\mathbf{l}}$, pointing from occluder toward receiver. For any object–receiver pair $(o, r) \in \mathcal{O} \times \mathcal{R}$ with 3D positions $\mathbf{O} = \mathbf{P}(o)$ and $\mathbf{R} = \mathbf{P}(r)$, we compute:

$$\mathbf{v} = \mathbf{R} - \mathbf{O}, \quad p = \mathbf{v} \cdot \mathbf{D}, \quad q^2 = \|\mathbf{v}\|_2^2 - p^2, \quad (2)$$

where \mathbf{v} is the displacement from the occluder point to the receiver point, p is the forward component of \mathbf{v} along the flow direction \mathbf{D} , and q^2 is the squared perpendicular component of \mathbf{v} with respect to \mathbf{D} .

We define that a receiver r is shadowed by object point o if it lies forward along \mathbf{D} and within an angular tolerance τ around \mathbf{D} :

$$p > 0 \quad \text{and} \quad q^2 \leq (\tan \tau)^2 p^2, \quad (3)$$

Equivalently, this enforces that the angle between \mathbf{v} and \mathbf{D} is at most τ . The estimate at r is then:

$$\text{estimate}(r) = \begin{cases} 1, & \exists o \in \mathcal{O} \text{ s.t. Eq. (3) holds,} \\ 0, & \text{otherwise.} \end{cases} \quad (4)$$

In practice we evaluate these dot products for all (o, r) pairs in parallel at 64×64 resolution and set $\text{estimate}(r) = 1$ if any object pixel satisfies the condition.

We then adopt a coarse-to-fine refinement strategy to predict the shadow mask. As depicted in Fig. 4, at the coarse stage (64×64), we concatenate the illumination-consistent shadow estimate, M_{fo} , and the point map \mathbf{P} with the denoising U-Net decoder features to produce a coarse map, which is then upsampled to 512×512 resolution.

At the fine stage, we concatenate the upsampled coarse map with the object mask, the point map, and a broadcast

3-channel light map, where each pixel repeats the predicted 3D light vector. A residual refinement block processes this stack and predicts a correction that is added to the coarse map, yielding the final shadow mask prediction, \tilde{M}_{fs} . We constrain the shadow mask loss as a combination of the BCE loss and the Dice [36] loss:

$$\mathcal{L}_{mask} = \text{BCE}(\tilde{M}_{fs}, \hat{M}_{fs}) + \lambda_1 \text{Dice}(\tilde{M}_{fs}, \hat{M}_{fs}), \quad (5)$$

where \hat{M}_{fs} is the ground-truth foreground shadow mask and λ_1 is a scalar weight.

3.4. Generation Process

The generative backbone is built on a frozen Stable Diffusion denoising U-Net, denoted $f(\cdot)$, conditioned by a ControlNet $g_\psi(\cdot)$. Given a timestep t and noise $\epsilon \sim \mathcal{N}(\mathbf{0}, \mathbf{I})$, we construct the noised latent

$$\mathbf{z}_t = \sqrt{\bar{\alpha}_t} \mathbf{z}_0 + \sqrt{1 - \bar{\alpha}_t} \epsilon, \quad (6)$$

and predict the additive Gaussian noise with the backbone using control features $\mathbf{c}_\psi = g_\psi(I_c, M_{fo}, \mathbf{P})$:

$$\hat{\epsilon}(\mathbf{z}_t, t, \mathbf{c}_\psi) = f(\mathbf{z}_t, t, \mathbf{c}_\psi). \quad (7)$$

The standard diffusion objective is

$$\mathcal{L}_{diff} = \mathbb{E} [\|\epsilon - \hat{\epsilon}(\mathbf{z}_t, t, \mathbf{c}_\psi)\|_2^2], \quad (8)$$

To capture the generated shadow intensity, we use a frozen intensity encoder from [23] that predicts per-latent-channel scale \mathbf{s} and bias \mathbf{b} from the composite image and background shadow mask. The background shadow mask is all zeros if there is no background object. Let $\mathbf{m} \in [0, 1]^{H \times W}$ denote the binarized predicted shadow mask. We modulate the predicted noise only in shadow regions:

$$\tilde{\epsilon}_\psi = (1 - \mathbf{m}) \odot \hat{\epsilon} + \mathbf{m} \odot (\mathbf{s} \odot \hat{\epsilon} + \mathbf{b}), \quad (9)$$

where \odot is element-wise multiplication. The training objective for generation becomes:

$$\mathcal{L}_{gen}(\psi) = \mathbb{E} [\|\epsilon - \tilde{\epsilon}_\psi\|_2^2], \quad (10)$$

Table 1. Comparison of baselines on DESOBAV2. We report global (G) and local (L, shadow-region) RMSE, SSIM, and BER for both BOS and BOS-free settings. GAN-based methods are pretrained on DESOBA, while diffusion-based methods are trained on DESOBAV2. Best scores are in **bold**.

Method	BOS						BOS-free					
	GRMSE↓	LRMSE↓	GSSIM↑	LSSIM↑	GBER↓	LBER↓	GRMSE↓	LRMSE↓	GSSIM↑	LSSIM↑	GBER↓	LBER↓
ShadowGAN[49]	8.681	70.459	0.961	0.174	0.470	0.938	19.146	87.149	0.903	0.052	0.483	0.961
Mask-SG[12]	10.450	73.776	0.938	0.186	0.485	0.966	19.662	89.637	0.895	0.054	0.488	0.972
AR-SG[22]	8.873	69.336	0.957	0.190	0.463	0.922	19.594	84.939	0.896	0.057	0.468	0.925
SGRNet[8]	9.017	71.582	0.961	0.189	0.446	0.887	20.883	85.841	0.894	0.056	0.450	0.881
SGDiffusion[23]	7.366	51.830	0.962	0.332	0.218	0.433	14.664	54.931	0.914	0.168	0.179	0.348
GPSD[51]	6.694	41.266	0.967	0.449	0.140	0.274	18.207	52.602	0.906	0.178	0.147	0.271
Ours	6.399	41.405	0.964	0.448	0.109	0.214	13.201	45.657	0.916	0.224	0.109	0.208

which updates only the ControlNet parameters ψ , while the denoising U-Net and intensity encoder remain frozen.

The total loss for the generation process is the sum:

$$\mathcal{L}_{total} = \mathcal{L}_{gen} + \mathcal{L}_{mask} + \lambda_2 \mathcal{L}_{lit}. \quad (11)$$

3.5. Point Map and Approximate Light Direction

For our framework, we use monocular geometry and an approximate light direction. Dense point maps are obtained per scene with the off-the-shelf MoGe-2 [41] model. We then estimate a single light direction by aligning a lightweight, differentiable shadow render to the observed shadow mask. In a camera-centric frame, we define the light as a unit vector:

$$\ell(\phi, \theta) = [-\cos \phi \cos \theta, -\sin \theta, -\sin \phi \cos \theta], \quad (12)$$

with azimuth ϕ and elevation θ , pointing toward the source. Using the object geometry and an estimated receiver plane $\Pi : (\mathbf{p} - \mathbf{p}_0) \cdot \mathbf{n} = 0$, candidate shadows are produced by ray-plane intersection from occluder points \mathbf{x}_i along $-\ell$:

$$t_i = \frac{(\mathbf{p}_0 - \mathbf{x}_i) \cdot \mathbf{n}}{(-\ell) \cdot \mathbf{n}}, \quad \mathbf{y}_i = \mathbf{x}_i + t_i(-\ell), \quad (13)$$

The resulting intersections \mathbf{y}_i are mapped into receiver coordinates and softly splatted to form a differentiable density R_ℓ . The light is obtained by minimizing a mask-matching objective with regularization for invalid casts:

$$\min_{\phi, \theta} \mathcal{L}(\phi, \theta) = 1 - \frac{2\langle R_\ell, M \rangle}{\|R_\ell\|_1 + \|M\|_1} + w\Omega, \quad (14)$$

where M is the observed shadow mask and Ω aggregates penalties, including negative t_i , back-facing rays, and off-receiver projections. We perform a coarse angular sweep followed by a gradient refinement to obtain the final approximate light direction, $(\hat{\phi}, \hat{\theta})$; we treat this optimized direction and its corresponding unit vector as supervision for the light predictor. The full pipeline is automated, and additional details are provided in the supplementary material.

4. Experiments and Results

Dataset and Evaluation Metrics. We conduct experiments on the DESOBAV2 [23] dataset, which contains 21,575 scenes with 28,573 image tuples. The dataset is split into 27,823 training tuples and 750 testing tuples. The test set covers two conditions: background-object-shadow (BOS), where background reference object-shadow pairs are present in the image; and BOS-free, where there is only a single object-shadow pair. We obtain per-image point maps from MoGe-2 [41] and derive 22,364 approximate light directions via our automated pipeline, which we use as supervision for light prediction when available.

For baselines, we compare with recent learning-based shadow generation methods, including GAN-based methods: ShadowGAN[49], MaskShadowGAN[12], ARShadowGAN[22], and SGRNet[8]. Note that we use their models pretrained on DESOBA and apply them directly to DESOBAV2. We also compare with SOTA diffusion-based methods, SGDiffusion[23] and GPSD[51], which are trained and evaluated on DESOBAV2. We evaluate both generated image quality and shadow mask accuracy. Following [23, 51], we report RMSE and SSIM for image quality, and BER for mask accuracy. All metrics are reported on the global image (G) and the local foreground-shadow region (L). Because diffusion models are stochastic, we generate five samples per test case with different random seeds and report the one with the highest local SSIM (LSSIM) against the ground truth.

Implementation Details. We implement our method in PyTorch [26]. The model is trained with the Adam [14] optimizer at a learning rate of 1×10^{-5} . We use the pre-trained denoising U-Net and intensity encoder from [23] and keep both frozen during training. The model is trained for 30 epochs on two NVIDIA RTX A6000 GPUs, with a batch size of 8. We set hyperparameter τ to 5° and λ_1, λ_2 to 0.1, 0.5, respectively. At inference, we use DDIM [34] with 25 steps and then apply the post-processing network from [23] as-is, without additional training. Further architectural and training details are provided in the supplementary material.

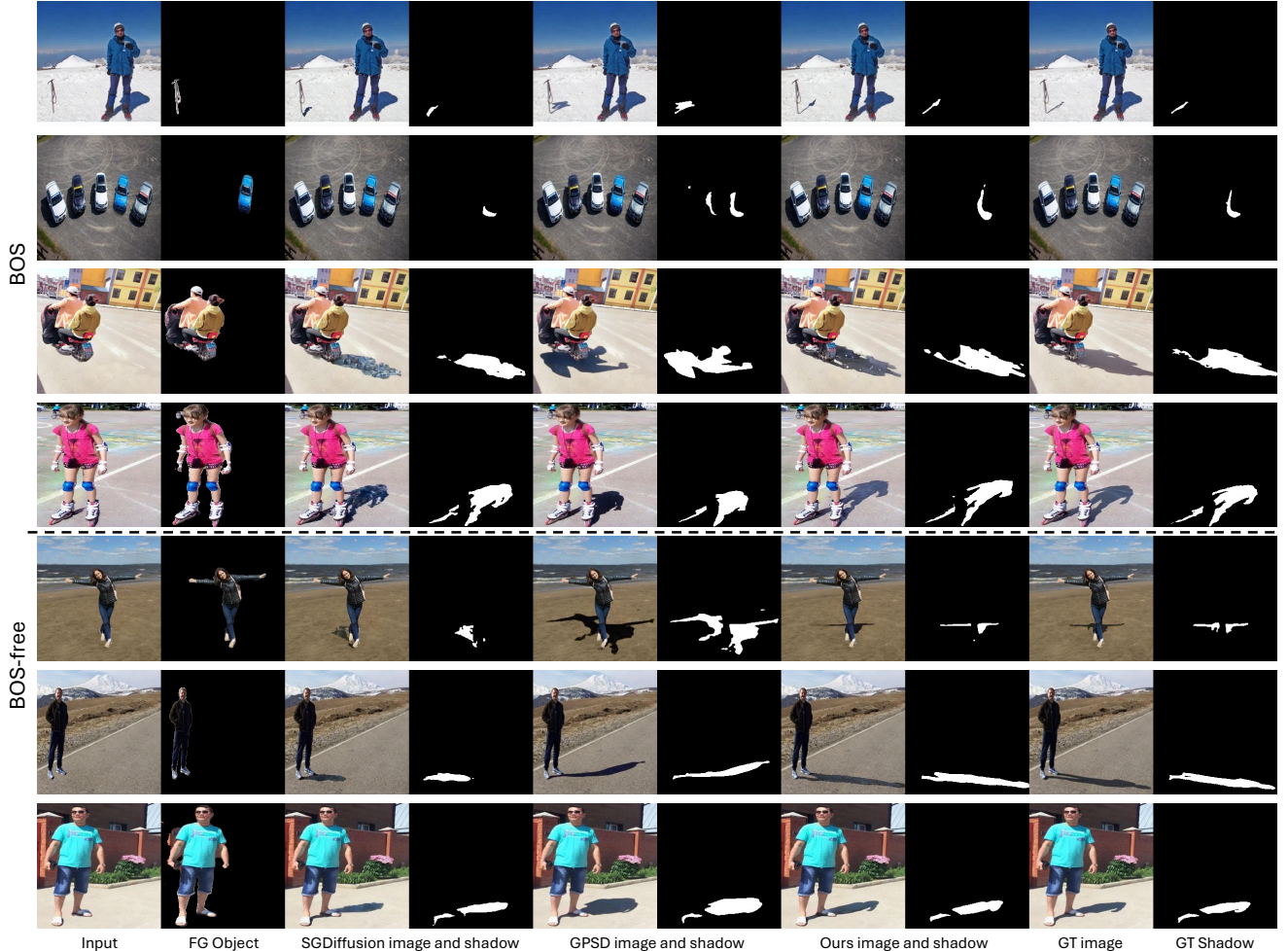


Figure 5. **Qualitative comparison with SOTA.** Visual results in both BOS (with background reference object–shadow pairs) and BOS-free (single object–shadow pair) settings. We compare generated images and predicted shadow masks against SGDiffusion[23], GPSD[51], and ground truth. Our method consistently produces higher image fidelity and more accurate shadow masks that better respect occluder–receiver–illumination relationships.

4.1. Comparisons with SOTA

Quantitative Results. On the DESOBAV2 test set (Tab. 1), our method achieves the best overall performance among nearly all baselines. In the BOS-free setting, we obtain the lowest global and local RMSE, the highest global and local SSIM, indicating consistently better reconstruction quality and shadow localization. In the BOS setting, our method achieves the lowest GRMSE, while remaining competitive in LRMSE and SSIM against GPSD. This is mainly because the shadows occupy a smaller fraction of the image, making SSIM less sensitive to local improvements. Overall, our generated images show reduced reconstruction error and strong local fidelity around the foreground shadow region. For mask accuracy, our method consistently improves over SOTA diffusion-based baselines in both settings. Compared to GPSD in the BOS split, our

GBER/LBER of 0.109/0.214 represent roughly a 22% relative reduction from 0.140/0.274, while in the BOS-free split our 0.109/0.208 improve over 0.147/0.271 by about 25–30%. These reductions indicate that the geometry- and light-aware, physics-grounded shadow estimate effectively suppresses false darkening and misalignment, yielding masks that better match the true occluder–receiver configuration under the predicted illumination.

Qualitative Results. Fig. 5 shows the qualitative comparisons against SGDiffusion [23] and GPSD [51]. We visualize both the generated images and the predicted masks. SGDiffusion often produces shadows with incomplete shapes and an incorrect inferred light direction, and its shadow intensities can be inconsistent with the scene illumination (rows 2, 3 and 6). GPSD leverages an object-conditioned shape prior, but as a learned prior it can hallucinate and drift, yielding incorrect shadow extents and

Table 2. Light prediction performance on DESOBAV2 test set. We report the count of scenes with valid approximate light directions in each setting and the mean angular error of our predictions.

Scene	Number	With Approximate	Mean Angular Error
BOS	500	375	3.829
BOS-free	250	235	8.689
All	750	610	5.701

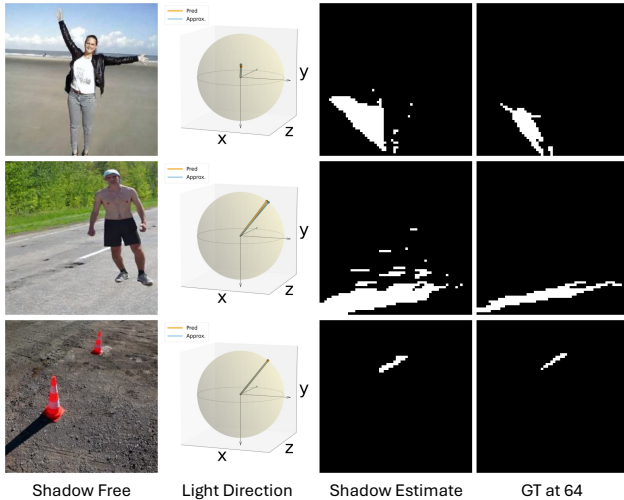


Figure 6. **Light prediction and Shadow Estimate.** Examples of predicted light directions and the resulting light-constrained shadow estimate. Light predictions match the approximates, and the estimate localizes shadows accurately while preserving shape.

topology (rows 1, 3, and 5). In contrast, our method anchors shadow location and shape with a physics-grounded estimate and then refines details at high resolution, leading to masks that align more closely with ground truth in both BOS and BOS-free settings. The resulting images also show better photometric consistency with the ground truth shadows. Overall, these results indicate stronger modeling of the occluder–receiver–illumination relationship, reducing misplacement and shape errors.

4.2. Light and Shadow Estimate

Tab. 2 summarizes light prediction accuracy. We report the mean angular error (in degrees) between our predicted directions and the approximate light targets. Overall, the error is below 6° , with better accuracy in the BOS setting, where background reference object-shadow pairs provide additional cues. We show the predicted light directions and their induced shadow estimates in Fig. 6. The predictions closely match the approximate directions derived from geometry, and the corresponding shadow estimates preserve shadow location accurately while capturing the coarse shape. During training, we deliberately disable the approximate light estimation for scenes with clearly spatially varying illumi-

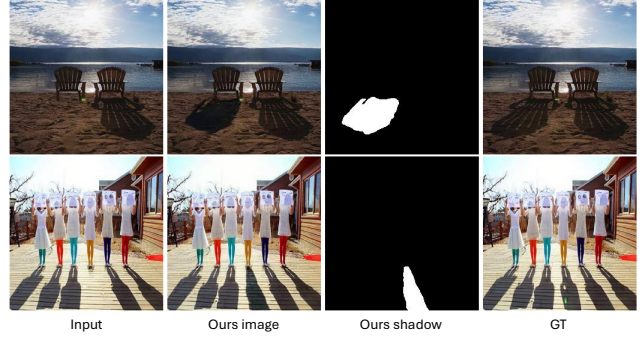


Figure 7. **Hard cases.** Examples where we disable approximate-light supervision during training: (top) spatially varying illumination and (bot) out-of-frame shadows. The model learns to predict reasonable lighting from data and produces plausible shadows.

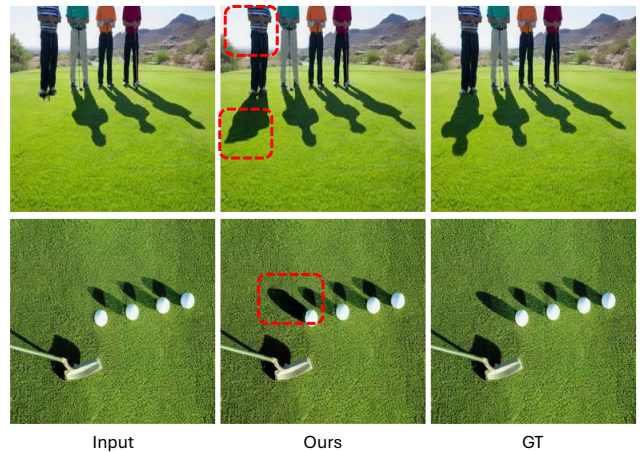


Figure 8. **Limitations.** *Top:* Failures from incomplete foreground object – our shadow estimate cannot hallucinate missing parts. *Bottom:* Intensity errors under multi-light illumination – the shadow is placed correctly but its intensity is off due to our single-light assumption.

nation and for cases with out-of-frame shadows, where a reliable elevation cannot be derived. However, our method still learns a foreground-object–focused light direction from data during training. As depicted in Fig. 7, the top row includes the sun in frame and shows spatially varying directions; yet our model correctly orients the cast shadow of the chair. The bottom row likewise demonstrates accurate light prediction and a plausible partial shadow on the receiver.

4.3. Ablation Study

We study the impact of our additional conditioning signals on the diffusion-based baseline. First, we experiment with geometry-only guidance over the baseline [23]. In Tab. 3, we compare the performance of the baseline model augmented with different geometry priors: relative depth maps from [44] versus metric point maps from [41]. Both geometry priors improve shadow generation performance. The depth-map-guided baseline yields better performance in the

Table 3. Comparisons of ablation studies. We compare our geometry-light-guided model against geometry-only-guided models. We report the RMSE, SSIM, and BER for both BOS and BOS-free settings. Best scores are in **bold**.

Method	BOS						BOS-free					
	GRMSE↓	LRMSE↓	GSSIM↑	LSSIM↑	GBER↓	LBER↓	GRMSE↓	LRMSE↓	GSSIM↑	LSSIM↑	GBER↓	LBER↓
SGDiffusion[23]	7.366	51.830	0.962	0.332	0.218	0.433	14.664	54.931	0.914	0.168	0.179	0.348
+ Depth Map	6.454	43.447	0.960	0.431	0.127	0.251	13.538	47.811	0.911	0.211	0.124	0.238
+ Point Map	6.280	42.549	0.964	0.424	0.135	0.267	13.286	46.168	0.915	0.220	0.114	0.216
Ours	6.399	41.404	0.964	0.448	0.109	0.214	13.201	45.657	0.916	0.224	0.109	0.208

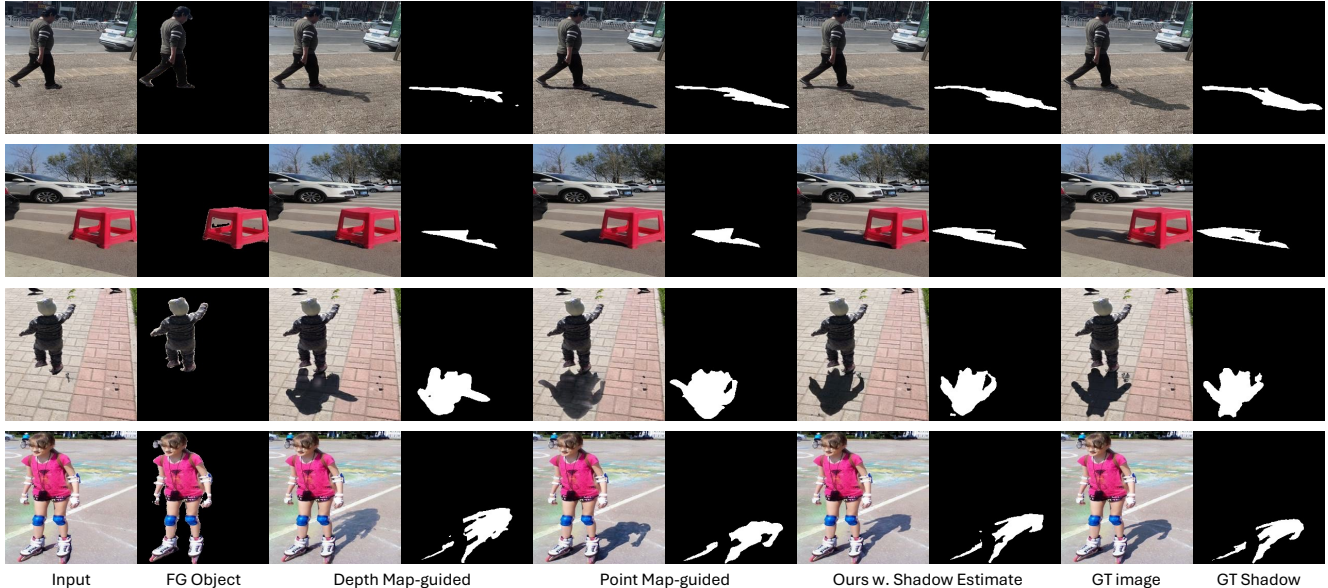


Figure 9. **Ablations.** Visual comparison of three variants of our method: (i) depth-guided, (ii) point map-guided, and (iii) proposed shadow-estimate-guided model. With extra illumination guidance, our method yields images that better align with scene geometry and produces shadow masks with more accurate shapes than geometry-only-guided variants.

BOS setting, with higher LSSIM and lower BER, while the point-map-guided baseline performs better in the BOS-free setting. This pattern reflects their representations: relative depth is image-consistent but lacks metric scale and offset, whereas the metric point map provides absolute 3D structure that better constrains contact regions and shadow extent. With extra illumination-guided cues, our method outperforms them on all metrics except GRMSE in the BOS setting. Fig. 9 shows the qualitative comparisons across configurations; our full model shows better photometric and geometric consistency and recovers finer shadow shapes.

5. Limitations

Although our method outperforms existing methods, there are still several limitations. First, since we rely on the foreground object geometry as a control signal and to build the shadow estimate, incomplete or erroneous geometry can lead to failure cases, as shown in Fig. 8 (first row). When the foreground object is only partially visible, our method cannot hallucinate the missing shape. The second row shows a failure case under multi-light conditions: although our

method correctly predicts the shadow’s location and shape, the resulting intensity is not correct. The primary reason is that we assume a single, shared light direction across the scene, and multi-light cases are rare in the dataset. Future work should address more complex lighting, such as indoor scenes with spatially varying illumination, and adopt more expressive light representations, for example, environment maps or area-light models that can better capture multi-source illumination.

6. Conclusion

We present a physics-guided shadow generation framework that conditions a diffusion backbone on monocular point-map geometry and an estimated single, scene-wide light direction vector. Following the shadow formation principle, we derive a shadow estimate from the geometry via an angular constraint, and then apply a coarse-to-fine refinement strategy to recover fine-grained shadow location and shape. By injecting this simple, explicit physics into the generation process, our method moves beyond purely 2D image-only mappings and enforces consistency between occluders, re-

ceivers, and illumination. Experiments on the DESOBAV2 benchmark, across both BOS and BOS-free settings, show that this design outperforms prior GAN- and diffusion-based approaches, yielding improved local shadow fidelity, reduced mask errors, and enhanced global image quality.

References

- [1] Jiayang Bai, Zhen He, Shan Yang, Jie Guo, Zhenyu Chen, Yan Zhang, and Yanwen Guo. Local-to-global panorama inpainting for locale-aware indoor lighting prediction. *IEEE Transactions on Visualization and Computer Graphics*, 29(11):4405–4416, 2023. 2
- [2] Eric Chan and Frédo Durand. Rendering fake soft shadows with smoothies. In *Rendering Techniques*, pages 208–218, 2003. 2
- [3] Zhihao Chen, Lei Zhu, Liang Wan, Song Wang, Wei Feng, and Pheng-Ann Heng. A multi-task mean teacher for semi-supervised shadow detection. In *Proceedings of the IEEE/CVF Conference on computer vision and pattern recognition*, pages 5611–5620, 2020. 2
- [4] Xiaodong Cun, Chi-Man Pun, and Cheng Shi. Towards ghost-free shadow removal via dual hierarchical aggregation network and shadow matting gan. In *Proceedings of the AAAI Conference on Artificial Intelligence*, pages 10680–10687, 2020. 2
- [5] Mohammad Reza Karimi Dastjerdi, Jonathan Eisenmann, Yannick Hold-Geoffroy, and Jean-François Lalonde. Everlight: Indoor-outdoor editable hdr lighting estimation. In *Proceedings of the IEEE/CVF international conference on computer vision*, pages 7420–7429, 2023. 2
- [6] Lanqing Guo, Siyu Huang, Ding Liu, Hao Cheng, and Bihan Wen. Shadowformer: global context helps shadow removal. In *Proceedings of the AAAI conference on artificial intelligence*, pages 710–718, 2023. 2
- [7] Lanqing Guo, Chong Wang, Wenhan Yang, Siyu Huang, Yufei Wang, Hanspeter Pfister, and Bihan Wen. Shadowdiffusion: When degradation prior meets diffusion model for shadow removal. In *Proceedings of the IEEE/CVF Conference on Computer Vision and Pattern Recognition*, pages 14049–14058, 2023. 2
- [8] Yan Hong, Li Niu, and Jianfu Zhang. Shadow generation for composite image in real-world scenes. *AAAI*, 2022. 5
- [9] Yan Hong, Li Niu, and Jianfu Zhang. Shadow generation for composite image in real-world scenes. In *Proceedings of the AAAI conference on artificial intelligence*, pages 914–922, 2022. 2
- [10] Shilin Hu, Hieu Le, ShahRukh Athar, Sagnik Das, and Dimitris Samaras. Shadow removal refinement via material-consistent shadow edges. In *2025 IEEE/CVF Winter Conference on Applications of Computer Vision (WACV)*, pages 2631–2641. IEEE, 2025. 2
- [11] Xiaowei Hu, Lei Zhu, Chi-Wing Fu, Jing Qin, and Pheng-Ann Heng. Direction-aware spatial context features for shadow detection. In *Proceedings of the IEEE conference on computer vision and pattern recognition*, pages 7454–7462, 2018. 2
- [12] Xiaowei Hu, Yitong Jiang, Chi-Wing Fu, and Pheng-Ann Heng. Mask-shadowgan: Learning to remove shadows from unpaired data. In *Proceedings of the IEEE/CVF international conference on computer vision*, pages 2472–2481, 2019. 1, 2, 5
- [13] Xiaowei Hu, Tianyu Wang, Chi-Wing Fu, Yitong Jiang, Qiong Wang, and Pheng-Ann Heng. Revisiting shadow detection: A new benchmark dataset for complex world. *IEEE Transactions on Image Processing*, 30:1925–1934, 2021. 2
- [14] Diederik P. Kingma and Jimmy Ba. Adam: A method for stochastic optimization. In *ICLR*, 2015. 5
- [15] Hieu Le and Dimitris Samaras. Shadow removal via shadow image decomposition. In *Proceedings of the IEEE/CVF International Conference on Computer Vision*, pages 8578–8587, 2019. 2
- [16] Hieu Le and Dimitris Samaras. From shadow segmentation to shadow removal. In *ECCV*, 2020.
- [17] Hieu Le and Dimitris Samaras. Physics-based shadow image decomposition for shadow removal. *IEEE Transactions on Pattern Analysis and Machine Intelligence*, 44(12):9088–9101, 2021. 2
- [18] Hieu Le, Tomas F Yago Vicente, Vu Nguyen, Minh Hoai, and Dimitris Samaras. A+ d net: Training a shadow detector with adversarial shadow attenuation. In *Proceedings of the European Conference on Computer Vision (ECCV)*, pages 662–678, 2018. 2
- [19] Hieu Le, Bento Goncalves, Dimitris Samaras, and Heather Lynch. Weakly labeling the antarctic: The penguin colony case. In *CVPR Workshops*, 2019. 2
- [20] Hieu Le, Dimitris Samaras, and Heather J. Lynch. A convolutional neural network architecture designed for the automated survey of seabird colonies. *Remote Sensing in Ecology and Conservation*, 8(2):251–262, 2022. 2
- [21] Ruofan Liang, Zan Gojcic, Merlin Nimier-David, David Acuna, Nandita Vijaykumar, Sanja Fidler, and Zian Wang. Photorealistic object insertion with diffusion-guided inverse rendering. In *European Conference on Computer Vision*, pages 446–465. Springer, 2024. 1
- [22] Daquan Liu, Chengjiang Long, Hongpan Zhang, Hanning Yu, Xinzhi Dong, and Chunxia Xiao. Arshadowgan: Shadow generative adversarial network for augmented reality in single light scenes. *CVPR*, pages 8136–8145, 2020. 2, 5
- [23] Qingyang Liu, Junqi You, Jianting Wang, Xinhao Tao, Bo Zhang, and Li Niu. Shadow generation for composite image using diffusion model. In *Proceedings of the IEEE/CVF Conference on Computer Vision and Pattern Recognition*, pages 8121–8130, 2024. 1, 2, 3, 4, 5, 6, 7, 8
- [24] Zhuang Liu, Hanzi Mao, Chao-Yuan Wu, Christoph Feichtenhofer, Trevor Darrell, and Saining Xie. A convnet for the 2020s. *Proceedings of the IEEE/CVF Conference on Computer Vision and Pattern Recognition (CVPR)*, 2022. 3
- [25] Jinting Luo, Ru Li, Chengzhi Jiang, Xiaoming Zhang, Mingyan Han, Ting Jiang, Haoqiang Fan, and Shuaicheng Liu. Diff-shadow: Global-guided diffusion model for shadow removal. In *Proceedings of the AAAI Conference on Artificial Intelligence*, pages 5856–5864, 2025. 2
- [26] Adam Paszke, Sam Gross, Francisco Massa, Adam Lerer, James Bradbury, Gregory Chanan, Trevor Killeen, Zeming

- Lin, Natalia Gimelshein, Luca Antiga, et al. Pytorch: An imperative style, high-performance deep learning library. *Advances in neural information processing systems*, 32, 2019. 5
- [27] Pakkapon Phongthawee, Worameth Chinchuthakun, Nontaphat Sinsunthithet, Varun Jampani, Amit Raj, Pramook Khungurn, and Supasorn Suwajanakorn. Diffusionlight: Light probes for free by painting a chrome ball. In *Proceedings of the IEEE/CVF conference on computer vision and pattern recognition*, pages 98–108, 2024. 2
- [28] Luigi Piccinelli, Yung-Hsu Yang, Christos Sakaridis, Mattia Segu, Siyuan Li, Luc Van Gool, and Fisher Yu. Unidepth: Universal monocular metric depth estimation. In *Proceedings of the IEEE/CVF Conference on Computer Vision and Pattern Recognition*, pages 10106–10116, 2024. 2
- [29] Liangqiong Qu, Jiandong Tian, Shengfeng He, Yandong Tang, and Rynson WH Lau. Deshadownet: A multi-context embedding deep network for shadow removal. In *Proceedings of the IEEE conference on computer vision and pattern recognition*, pages 4067–4075, 2017. 2
- [30] Robin Rombach, Andreas Blattmann, Dominik Lorenz, Patrick Esser, and Björn Ommer. High-resolution image synthesis with latent diffusion models. In *Proceedings of the IEEE/CVF conference on computer vision and pattern recognition*, pages 10684–10695, 2022. 3
- [31] Michael Schwarz and Marc Stamminger. Bitmask soft shadows. In *Computer Graphics Forum*, pages 515–524. Wiley Online Library, 2007. 2
- [32] Yichen Sheng, Yifan Liu, Jianming Zhang, Wei Yin, A Cengiz Oztireli, He Zhang, Zhe Lin, Eli Shechtman, and Bedrich Benes. Controllable shadow generation using pixel height maps. In *European Conference on Computer Vision*, pages 240–256. Springer, 2022. 2
- [33] Gowri Somanath and Daniel Kurz. Hdr environment map estimation for real-time augmented reality. In *Proceedings of the IEEE/CVF conference on computer vision and pattern recognition*, pages 11298–11306, 2021. 2
- [34] Jiaming Song, Chenlin Meng, and Stefano Ermon. Denoising diffusion implicit models. *arXiv preprint arXiv:2010.02502*, 2020. 5
- [35] Yizhi Song, Zhifei Zhang, Zhe Lin, Scott Cohen, Brian Price, Jianming Zhang, Soo Ye Kim, and Daniel Aliaga. Object-stitch: Object compositing with diffusion model. In *Proceedings of the IEEE/CVF Conference on Computer Vision and Pattern Recognition*, pages 18310–18319, 2023. 1
- [36] Carole H Sudre, Wenqi Li, Tom Vercauteren, Sebastien Ourselin, and M Jorge Cardoso. Generalised dice overlap as a deep learning loss function for highly unbalanced segmentations. In *International Workshop on Deep Learning in Medical Image Analysis*, pages 240–248. Springer, 2017. 4
- [37] Minghui Tan, Jean-François Lalonde, Lavanya Sharan, Holly Rushmeier, and Carol O’Sullivan. The perception of lighting inconsistencies in composite outdoor scenes. *ACM Transactions on Applied Perception (TAP)*, 12(4):1–18, 2015. 1
- [38] Joanna Tarko, James Tompkin, and Christian Richardt. Real-time virtual object insertion for moving 360 videos. In *Proceedings of the 17th ACM SIGGRAPH International Conference on Virtual-Reality Continuum and its Applications in Industry*, pages 1–9, 2019. 1
- [39] Dor Verbin, Ben Mildenhall, Peter Hedman, Jonathan T Barron, Todd Zickler, and Pratul P Srinivasan. Eclipse: Disambiguating illumination and materials using unintended shadows. In *Proceedings of the IEEE/CVF Conference on Computer Vision and Pattern Recognition*, pages 77–86, 2024. 2
- [40] Jifeng Wang, Xiang Li, and Jian Yang. Stacked conditional generative adversarial networks for jointly learning shadow detection and shadow removal. In *Proceedings of the IEEE conference on computer vision and pattern recognition*, pages 1788–1797, 2018. 2
- [41] Ruicheng Wang, Sicheng Xu, Yue Dong, Yu Deng, Jianfeng Xiang, Zelong Lv, Guangzhong Sun, Xin Tong, and Jiaolong Yang. Moge-2: Accurate monocular geometry with metric scale and sharp details, 2025. 2, 5, 7
- [42] Yonghui Wang, Shaokai Liu, Li Li, Wengang Zhou, and Houqiang Li. Swinshadow: Shifted window for ambiguous adjacent shadow detection. *ACM Transactions on Multimedia Computing, Communications and Applications*, 2024. 2
- [43] Lihe Yang, Bingyi Kang, Zilong Huang, Xiaogang Xu, Jiashi Feng, and Hengshuang Zhao. Depth anything: Unleashing the power of large-scale unlabeled data. In *Proceedings of the IEEE/CVF Conference on Computer Vision and Pattern Recognition*, pages 10371–10381, 2024. 2
- [44] Lihe Yang, Bingyi Kang, Zilong Huang, Zhen Zhao, Xiaogang Xu, Jiashi Feng, and Hengshuang Zhao. Depth anything v2. *Advances in Neural Information Processing Systems*, 37:21875–21911, 2024. 2, 7
- [45] Wei Yin, Chi Zhang, Hao Chen, Zhipeng Cai, Gang Yu, Kaixuan Wang, Xiaozhi Chen, and Chunhua Shen. Metric3d: Towards zero-shot metric 3d prediction from a single image. In *Proceedings of the IEEE/CVF international conference on computer vision*, pages 9043–9053, 2023. 2
- [46] Dongxu Yue, Maomao Li, Yunfei Liu, Qin Guo, Ailing Zeng, Tianyu Yang, and Yu Li. Addme: Zero-shot group-photo synthesis by inserting people into scenes. In *European Conference on Computer Vision*, pages 222–239. Springer, 2024. 1
- [47] Jinsong Zhang, Kalyan Sunkavalli, Yannick Hold-Geoffroy, Sunil Hadap, Jonathan Eisenman, and Jean-François Lalonde. All-weather deep outdoor lighting estimation. In *Proceedings of the IEEE/CVF conference on Computer Vision and Pattern Recognition*, pages 10158–10166, 2019. 2
- [48] Lvmin Zhang, Anyi Rao, and Maneesh Agrawala. Adding conditional control to text-to-image diffusion models. In *Proceedings of the IEEE/CVF international conference on computer vision*, pages 3836–3847, 2023. 2
- [49] Shuyang Zhang, Runze Liang, and Miao Wang. Shadowgan: Shadow synthesis for virtual objects with conditional adversarial networks. *Computational Visual Media*, 5(1):105–115, 2019. 1, 5
- [50] Yuhong Zhang, Han Wang, Yiwen Wang, Rong Xie, and Li Song. Freeinsert: Personalized object insertion with geometric and style control. In *Proceedings of the 33rd ACM International Conference on Multimedia*, pages 10361–10369, 2025. 1

- [51] Haonan Zhao, Qingyang Liu, Xinhao Tao, Li Niu, and Guangtao Zhai. Shadow generation using diffusion model with geometry prior. In *Proceedings of the Computer Vision and Pattern Recognition Conference*, pages 7603–7612, 2025. [1](#), [2](#), [5](#), [6](#)
- [52] Lei Zhu, Zijun Deng, Xiaowei Hu, Chi-Wing Fu, Xuemiao Xu, Jing Qin, and Pheng-Ann Heng. Bidirectional feature pyramid network with recurrent attention residual modules for shadow detection. In *Proceedings of the European Conference on Computer Vision (ECCV)*, pages 121–136, 2018. [2](#)
- [53] Lei Zhu, Ke Xu, Zhanghan Ke, and Rynson WH Lau. Mitigating intensity bias in shadow detection via feature decomposition and reweighting. In *Proceedings of the IEEE/CVF International Conference on Computer Vision*, pages 4702–4711, 2021. [2](#)